

Self-Supervised Data-Driven Approach Defines Pathological High-Frequency Oscillations in Human

Authors: Yipeng Zhang¹, Atsuro Daida², Lawrence Liu¹, Naoto Kuroda³, Yuanyi Ding¹, Shingo Oana², Sotaro Kanai², Tonmoy Monsoor¹, Chenda Duan¹, Shaun A. Hussain^{2,4}, Joe X Qiao⁵, Noriko Salamon⁵, Aria Fallah⁶, Myung Shin Sim⁷, Raman Sankar^{2,4}, Richard J. Staba⁸, Jerome Engel Jr.⁸⁻¹¹, Eishi Asano³, Vwani Roychowdhury¹*, Hiroki Nariai^{2,4*}

¹ Department of Electrical and Computer Engineering, University of California, Los Angeles, CA, USA

² Division of Pediatric Neurology, Department of Pediatrics, UCLA Mattel Children's Hospital, David Geffen School of Medicine, Los Angeles, CA, USA

³ Department of Pediatrics and Neurology, Children's Hospital of Michigan, Wayne State University School of Medicine, Detroit, MI, USA

⁴ The UCLA Children's Discovery and Innovation Institute, Los Angeles, CA, USA

⁵ Division of Neuroradiology, Department of Radiology, UCLA Medical Center, David Geffen School of Medicine, Los Angeles, CA, USA

⁶ Department of Neurosurgery, UCLA Medical Center, David Geffen School of Medicine, Los Angeles, CA, USA

⁷ Department of Medicine, Statistics Core, University of California, Los Angeles, CA, USA

⁸ Department of Neurology, UCLA Medical Center, David Geffen School of Medicine, Los Angeles, CA, USA

⁹ Department of Neurobiology, University of California, Los Angeles, CA, USA

¹⁰ Department of Psychiatry and Biobehavioral Sciences, University of California, Los Angeles, CA, USA

¹¹ The Brain Research Institute, University of California, Los Angeles, CA, USA

Character count title: 94 characters (including space)
Word count abstract: 246 words
Word count text total: 4413 words (Introduction, Methods, Results, and Discussion)
Number of Tables: 2 for print, 4 for supplementary data
Number of Figures: 6 for print, 13 for supplementary data
Running Title: Self-supervised HFO classification in epilepsy

***Corresponding author:**

Hiroki Nariai, MD, PhD, MS (hnariai@mednet.ucla.edu) and Vwani Roychowdhury (vwani@g.ucla.edu)

Key words: HFO, pathological HFOs, artificial intelligence, self-supervised learning, machine learning

Abbreviations: HFOs: high-frequency oscillations. EEG: electroencephalogram. mpHFOs: morphologically defined putative pathological HFOs. SOZ: seizure onset zone. EZ: epileptogenic zone. iEEG: intracranial EEG. SEEG: stereotactic EEG. DL: deep learning. VAE: variational autoencoder. mArtifacts: Artifacts defined based on morphological analysis using the VAE model. spkHFOs: HFOs with spikes. non-spkHFOs: HFOs without spikes. HS: hippocampal sclerosis. FCD: focal cortical dysplasia. t-SNE: t-distributed stochastic neighbor embedding. ROIs: regions of interest. AUC: area under the curve. CT: computed tomography. MRI: magnetic resonance imaging. RMS: root mean square. SD: standard deviation. STE: short-term energy. IQR: interquartile range

ABSTRACT

Objective: Interictal high-frequency oscillations (HFOs) are a promising neurophysiological biomarker of the epileptogenic zone (EZ). However, objective criteria for distinguishing pathological from physiological HFOs remain elusive, hindering clinical application. We investigated whether the distinct mechanisms underlying pathological and physiological HFOs are encapsulated in their signal morphology in intracranial EEG (iEEG) recordings and whether this mechanism-driven distinction could be simulated by a deep generative model.

Methods: In a retrospective cohort of 185 epilepsy patients who underwent iEEG monitoring, we analyzed 686,410 HFOs across 18,265 brain contacts. To learn morphological characteristics, each event was transformed into a time-frequency plot and input into a variational autoencoder. We characterized latent space clusters containing morphologically defined putative pathological HFOs (mpHFOs) using interpretability analysis, including latent space disentanglement and time-domain perturbation.

Results: mpHFOs showed strong associations with expert-defined spikes and were predominantly located within the seizure onset zone (SOZ). Discovered novel pathological features included high power in the gamma (30–80 Hz) and ripple (>80 Hz) bands centered on the event. These characteristics were consistent across multiple variables, including institution, electrode type, and patient demographics. Predicting 12-month postoperative seizure outcomes using the resection ratio of mpHFOs outperformed unclassified HFOs (F1=0.72 vs. 0.68) and matched current clinical standards using SOZ resection (F1=0.74). Combining mpHFO data with demographic and SOZ resection status further improved prediction accuracy (F1=0.83).

Interpretation: Our data-driven approach yielded a novel, explainable definition of pathological HFOs, which has the potential to further enhance the clinical use of HFOs for EZ delineation.

INTRODUCTION

Over a third of epilepsy patients do not respond to medication and may become candidates for epilepsy surgery. Currently, surgical plans mainly rely on neuroimaging and EEG, including interictal spikes and the seizure onset zone (SOZ), but seizure freedom rates remain around 50–85%.¹ Discovering a biomarker to precisely delineate the epileptogenic zone (EZ: the brain regions responsible for generating seizures) would be transformative. Interictal high-frequency oscillations (HFOs) in intracranial EEG (iEEG) show promise as spatial biomarkers for delineating the epileptogenic zone (EZ),²⁻⁴ with studies linking HFO-generating regions' removal to postoperative seizure freedom.^{5,6} However, using HFOs in surgery is challenging because they can arise from both pathological and physiological sources, and currently, no method exists to reliably distinguish between the two.⁷

Supervised machine learning is highly effective when human annotators accurately label large-scale datasets. Deep learning (DL) models can learn complex patterns representative of labeled categories and then perform automated classification on unseen signals and images with high accuracy.⁸ For HFO classification, certified experts would be required to annotate large repositories of HFOs from diverse groups of patients accurately and consistently. However, accurately labeling pathological HFOs is challenging due to a lack of consensus on their definition. Recent studies^{9,10} have explored weakly supervised approaches where, instead of expert labels, clinical evidence based on seizure freedom and channel resection status can be used to train DL models. However, these methods have limited scalability since clinical evidence is not always available, especially in stereotactic EEG (SEEG) without resection. Additionally, labeling, such as SOZ annotation and resection margin determination, lacks standardization across institutions and may be inaccurate.^{11,12}

A potential solution to the limitations of supervised learning is to utilize original observations. Research using microelectrodes indicates that pathological HFOs, generated by abnormal synchronous burst firing, are morphologically distinct from physiological HFOs, which stem from inhibitory synchronous postsynaptic potentials.^{7,13} However, clinical iEEG recordings often use macroelectrodes, and traditional signal processing algorithms have been insufficient in characterizing these morphological differences.^{14,15} A generative AI model, like a variational autoencoder (VAE),¹⁶ can capture subtle morphological differences based on such biological mechanisms without labels if given a large dataset. VAEs, trained in a self-supervised manner, have proven effective in natural language processing,¹⁷ computer vision,^{18,19} and EEG analysis.^{20,21} They learn low-dimensional representations by reconstructing data from latent codes, forming clusters in latent space that capture different data-generative mechanisms. Once the morphological characteristics of pathological HFOs are learned, they can be visualized and interpreted through latent space exploration.

This study utilized a large multi-institutional cohort of patients who underwent iEEG monitoring with grid or SEEG electrodes, providing comprehensive coverage of deep and superficial brain regions. We developed a VAE framework to analyze large numbers of HFOs and identify morphologically defined putative pathological HFOs (mpHFOs). Using the interpretability of VAEs, we explored various neurophysiological characteristics of mpHFOs through the VAE's latent space disentanglement. Finally, we tested postoperative seizure outcome prediction using the mpHFO resection ratio from interictal EEG recordings to assess its comparability to the current clinical standard of SOZ-based prediction.

METHODS:

Patient cohort: This was a multi-institutional retrospective cohort study. The inclusion criteria consisted of [a] simultaneous video-iEEG recording for epilepsy surgery from August 2016 to December 2023 at UCLA Mattel Children's Hospital (UCLA grid/strip and UCLA SEEG cohorts) or from January 2007 to May 2018 at Children's Hospital of Michigan, Detroit, (Detroit grid/strip cohort) [b] iEEG sampling rate of at least 1,000Hz, [c] iEEG contained at least an artifact-free 5 min slow-wave sleep epoch at least two hours apart from clinical seizure events, and [d] known postoperative seizure outcomes over one year for patients who had resective surgery. The exclusion criteria included [a] undergoing hemispherectomy or hemispherotomy and [b] the presence of massive brain malformations (such as megalencephaly and perisylvian polymicrogyria) or previous surgeries that make it difficult to identify brain anatomy during the iEEG study. The institutional review board at UCLA and Wayne State University have approved the protocol. We obtained written informed consent from patients or the guardians of pediatric patients.

Patient evaluation: All patients with medically refractory epilepsy referred during the study period underwent a standardized presurgical evaluation.^{9,22} The margins and extent of resections were determined mainly based on the SOZ, clinically defined as regions initially exhibiting sustained rhythmic waveforms at the onset of habitual seizures. Postoperative seizure outcomes were determined based on the status of Engel class I outcomes versus others 12 months after the resective surgery.

iEEG recording: Macroelectrodes, including platinum grid electrodes (10 mm intercontact distance) and depth electrodes (platinum, 5 mm intercontact distance), were surgically implanted. The placement of intracranial electrodes was guided by the results of scalp video-EEG recording and neuroimaging studies. Regarding the SEEG placement, BrainLab Elements software was used for planning the electrodes to the intended targets using T1-weighted sequences, and the trajectories were guided by a gadolinium-enhanced T1-weighted MRI. Both institutions obtained iEEG recordings using Nihon Kohden Systems (Irvine, California, USA). The sampling frequency was set at 1,000 Hz in Detroit and at 2,000 Hz in UCLA upon acquisition.

Acquisition of three-dimensional (3D) brain surface images: We obtained preoperative high-resolution 3D magnetization-prepared rapid acquisition with gradient echo (MPRAGE) T1-weighted image of the entire head. Using the FreeSurfer scripts, we created the averaged surface image to which all electrode locations were spatially normalized.^{9,22} In cases where the software failed to detect the pial surface accurately due to insufficient cerebral myelination, we manually delineated the pial surface using the Control Point function. The averaged surface image functioned as the template for the analysis of anatomical location.

Anatomical labeling and determination of ROIs: For the dataset from UCLA, each implanted contact was labeled visually according to the Desikan-Killiany-Tourville atlas.²³ The location of electrodes was directly defined within a Freesurfer-based 3D surface image using post-implant computed tomography (CT) images using Brainstorm software.⁹ For the dataset from Detroit, all implanted subdural contacts were coregistered with 3D surface images within the FreeSurfer with an FSaverage vertex label.²² We defined 34 regions of interest (ROIs) for further analysis (**Table 2**). For the data harmonization between the two institutions, the FSaverage vertex of Detroit datasets was converted to MNI coordinates.²⁴ Finally, these data were combined with UCLA patients, which were projected to the MNI normalized space under Brainstorm for the co-registration image (**Figure 1a**).

iEEG data pre-processing: We used a customized common average reference for the grid⁹ and a bipolar montage for SEEG data. The EEG was first resampled to be the same sampling frequency of 1,000 Hz, and a band-reject filter was to reject the 60 Hz and its harmonics with a stopband of 2 Hz. iEEG channels not recording from grey matter (e.g., located outside of the brain) or otherwise deemed 'bad' (e.g., excessively noisy or artifactual) by the clinicians were discarded from the analysis.

Automated HFO detection: HFOs were detected by the PyHFO platform using both STE and MNI detectors to enhance the sensitivity of detection.^{25,26} For both detectors, previously published default parameters were used (**Supplementary Table 3**), except the frequency band was adjusted to 80-300 Hz to accommodate sampling frequency of 1,000 Hz. Each event was classified into an artifact, HFO with spike (spkHFO), and HFO without spike (non-spkHFO) using the released deep learning models from PyHFO.

Overall training and inference method: **Figure 1** and **Supplementary Figure 1-3** outline the overall study flow.

Morphology-based pathological HFO classification by deep generative model

Subject-wise k-fold Cross-validation: To thoroughly test our method, we used a subject-wise five-fold cross-validation. Specifically, for each fold, we set aside 20% of the subjects as a test set (controlling sampling from UCLA grid/strip, UCLA SEEG, and Detroit grid/strip, ensuring every subject was tested once over five folds). All

remaining subjects became the training set. Within the training set, we randomly sampled ten subjects from each dataset as the validation set.

Feature Representation: Each event detected by the automatic detector was represented by a time-frequency plot (Morlet wavelet transform), known for capturing the morphological information of HFO events.⁹ The plot spans ± 285 ms (centered on the HFO event) and covers frequencies from 10 to 290 Hz. It was resized to a 64 x 64 resolution and normalized to a range of 0 to 1 as the input of VAE.

Self-supervised VAE training: The VAE encodes input images as latent code distributions and samples from them during decoding, allowing it to reproduce input images and generate similar new images (**Figure 1b**, **Supplementary Figure 1**). The self-supervised loss function includes reconstruction loss and variational regularization, which ensures the latent space follows a normal distribution. We used ResNet54 as the backbone for both the encoder and decoder, inspired by its success in capturing morphological features in time-frequency plots.²⁷ The latent space was set to 8 dimensions, and an ablation study with 16 dimensions showed increased redundancy (**Supplementary Figure 8**).

We trained our VAE over 80 epochs to reconstruct input images, using the Adam optimizer with a learning rate of 3×10^{-4} and a batch size of 512. To enhance the model's generalization ability, we augmented the time-frequency plots by randomly flipping them along the time axis. Stratified sampling was employed to ensure even subject representation, capping the number of samples at 2,500 per subject per epoch. We selected perceptual loss as the reconstruction criterion to capture morphological discrepancies between input and output images more effectively. To achieve a more disentangled latent space, we adopted beta-VAE, using the loss function: **loss = perceptual loss + $\beta \times$ KL divergence**, with $\beta = 0.1$. At each training epoch, we monitored validation loss and selected the model checkpoint with the lowest validation loss for constructing the classifier and performing inference.

Unsupervised discovery of HFO clusters: We developed a hierarchical two-stage Gaussian Mixture Model (GMM) clustering pipeline to identify morphologically distinct classes of HFOs (**Figure 1c**, **Supplementary Figure 1**). We extracted latent codes from the training dataset using VAE's encoder. In the first stage, we applied GMM clustering with $k=2$, using stratified sampling to balance subject contributions by capping events at 10,000 per subject. The cluster with high reconstruction loss was identified as artifacts (mArtifacts) due to their diverse morphologies and poor reconstruction by the VAE. In the second stage, we further clustered the non-artifact events into two clusters using another GMM, capping events at 2,000 per subject. To assign pathological (mpHFO) or physiological (non-mpHFO) labels to these clusters, we minimally used clinical data: the cluster with a higher resection percentage in seizure-free patients was deemed pathological. An ablation study exploring different

stratified sampling methods showed similar performance in predicting surgical outcomes (**Supplementary Figure 9**).

HFO morphology inference pipeline: To predict new HFO events, time-frequency plots were computed and latent codes were extracted by VAE encoder. The trained hierarchical GMM then predicted each latent code, assigning class label (mpHFO/non-mpHFO/mArtifact) to each event.

Interpretability analysis:

We conducted an interpretability analysis of HFO classification within the VAE model. Pixel-wise t-tests on time-frequency plots extracted from the trained model were performed to identify distinct morphological characteristics of mpHFOs. Latent space visualization (t-SNE) and classification evaluated demographic and anatomical factors impacting HFO morphology. By latent space disentanglement and latent dimension perturbation, we aimed to map each latent dimension to meaningful neurophysiological characteristics and identify specific latent dimensions related to pathological features of mpHFOs. Time-domain perturbation was also performed to examine gamma-band activity's role in HFO morphology. Further details of the interpretability analysis are described in the **Supplementary Methods** Section.

Clinical correlation: Predicting surgical outcomes:

We assessed the effectiveness of the mpHFO by extracting subject-specific features and training predictive models to determine postoperative seizure-free outcomes in subjects who underwent resection following iEEG monitoring with grid or strip electrodes. Key features included the resection ratio (number of events including in the resected brain regions divided by the total number of detected events; we merged overlapped events between STE and MNI detectors in the calculation, **Supplementary Table 4**), demographic data such as sex and age, and the resection status of SOZ, which is a clinical standard for guiding epilepsy surgery. We employed two validation approaches. First, we evaluated the separation between seizure-free and non-seizure-free subjects in the feature space and assessed the balance of performance across five-fold cross-validation (i.e., seizure-free subjects should have a higher resection ratio in all folds and vice versa.). We trained single and multivariable logistic regression models on features from all test sets and compared their area under the curve (AUC). Additionally, we employed a non-linear predictive model (random forest) (**Figure 6c**) aiming to forecast postoperative seizure freedom based on subject-specific features identified through subject-wise five-fold cross-validation (**Supplementary Figure 3**). To better assess performance given the label imbalance, we reported both accuracy and the F1 score, including their respective means and standard errors of the mean.

Statistical analysis:

Statistical analyses were performed using Python (3.9.1), and the deep neural network was developed in PyTorch (2.1.0). Quantitative data are reported as medians with interquartile ranges or means with standard deviations. Group comparisons used chi-square tests for distributions and Student's t-tests for means, with significance set at $p < 0.05$ unless stated otherwise. Machine learning model performance was evaluated using accuracy and F1 score. Specific statistical tests for each experiment are detailed in their respective sections.

RESULTS

Cohort characteristics:

We studied 185 patients (91 females) from two centers who met the eligibility criteria (**Table 1**). The median age at surgery was 13 years (range: 2–44 years). A total of 18,265 artifact-free electrode sites (median: 106 per patient; range: 29–152) within 34 ROIs were available for analysis (**Figure 1a**). There were 1,670 electrode sites sampled within the SOZ and 7,960 sites sampled within non-epileptogenic brain regions, defined as spared brain regions in patients with postoperative seizure freedom (**Table 2**). The median duration of analyzed EEG data for the UCLA grid/strip dataset was 91.5 min [IQR: 90.6-94.8 min], and for the UCLA SEEG, it was 90.3 minutes [IQR: 87.1-96.8 min]. The median analyzed EEG recording duration for the Detroit grid/strip dataset was 5.3 minutes [IQR: 5.1-5.7 min]. In total, 686,410 putative HFOs were detected from all the datasets. The median rate of HFOs (number of detections/min) within SOZ contacts was 3.11 (range: 0.73-7.17), and the median rate of HFOs within the non-epileptogenic contacts was 1.08 (range: 0.63-2.15) across the ROIs. There were 162 patients who underwent resective surgery, and 113 patients (69.8 %) achieved seizure freedom. Of the patients who had resection, pathology results were as follows: focal cortical dysplasia (FCD) (41.4%), hippocampal sclerosis (HS) (6.8%), tumor (19.1%), and others (32.7%).

Characterization of pathological HFOs based on the self-supervised VAE algorithm:

With five-fold subjective-wise cross-validation, 80.1% of the mpHFOs were classified as spkHFOs, 84.87 % of the non-mpHFOs were classified as non-spkHFOs, and 93.56% of mArtifacts were classified as artifactual HFOs. Clustering results were visualized on a two-dimensional plane and were consistent across folds (**Figure 2a,b; Supplementary Figure 4**). Moreover, the mpHFO rate (count/channel/min) was significantly higher than the non-mpHFO rate (count/channel/min) in the SOZ channels across three datasets ($p < 0.05$) and did not exhibit significant difference within the non-SOZ channels (Detroit grid/strip: $p = 0.1$, UCLA SEEG: $p = 0.49$, UCLA grid/strip: $p = 0.38$) (**Figure 2c**). The morphological analysis demonstrated that mpHFOs had higher amplitude values throughout the HFO band (≥ 80 Hz), around the center (detection) point (0 ms, where HFOs

were detected) than non-mpHFOs (**Figure 2d, e**). Furthermore, there were statistically higher values of mpHFOs at the sub-HFO band (10-80 Hz) throughout the time window compared to non-mpHFOs. These bands together lead to a cone-shaped template in the time-frequency plot (**Figure 2e**). Such a template showed consistency regardless of the variables, including sex, the origin of the dataset, pathology, and age categories (**Supplementary Figure 5**). The application of a 10-80 Hz bandpass filter revealed spike-like EEG signals in mpHFOs (**Figures 2f–h**), which were absent in non-mpHFOs (**Figures 2i–k**).

HFO morphology analysis based on dataset origin, sex, age, and pathology:

We analyzed whether HFO morphology was influenced by recording sites/type (UCLA grid/strip, UCLA SEEG, Detroit grid/strip), sex (female vs. male), age (0-5, 6-10, 11-15, 16-20, and 21+), and pathology (HS, FCD, Tumor, others). We projected latent codes of HFOs into 2D space, color-coded by subcategories (**Figure 3a, c, e, g**). A statistical test (**Supplementary Method**) showed there was no significant differentiation in HFO morphology based on dataset sources ($p = 0.13$), sex ($p = 0.44$), age ($p = 0.10$), or pathology ($p = 0.83$) (**Figure 3b, d, f, h**).

HFO morphology analysis based on ROIs (anatomical location):

We analyzed whether HFOs from different anatomical locations (frontal, temporal, parietal, occipital, limbic) exhibit distinguishable morphologies. A latent space plot of HFOs from the preserved regions in patients who remained seizure-free after resection, presumably physiological HFOs, revealed a cluster from the occipital region (**Figure 4a, b**). A statistical test (**Supplementary Method**) showed a classifier could distinguish these occipital HFOs with 62% accuracy (**Figure 4c**). Averaged time-frequency plots showed distinct peak frequency and power ratios for occipital HFOs compared to other regions (**Supplementary Figure 6**). However, HFOs from the SOZ, presumably pathological HFOs, did not show significant morphological differences across anatomical locations (**Figure 4e-h**).

Disentanglement of the latent space to establish neurophysiological characteristics of pathological HFOs:

We visualized each dimension of the latent space using boxplots to compare mpHFO and non-mpHFO groups. Some dimensions showed different distributions between these two groups (**Supplementary Figure 7**). With the latent space interpretation, we identified a dimension that separated mpHFOs from non-mpHFOs. Interpolating this specific dimension resulted in generated images with increased power within the gamma band

and HFO band within the cone-shaped template (**Figure 5a, b**). At the population level, interpolating this dimension led to decoded images showing increased power in both the gamma and HFO bands within the cone-shaped template region (**Figure 5c, Supplementary Figure 10**). Predicting these images by the inference pipeline demonstrated that the model confidence toward mpHFOs increased as the value of this dimension increased (**Figure 5d**). Although we identified dimensions representing beta band power and peak frequency, their latent space interpolation did not affect the model confidence toward mpHFOs (**Figure 5e-h, Supplementary Figure 11**). With the time-domain perturbations on the original signals, we demonstrated that decreasing the frequency of the signal in the sub-HFO band (10-80 Hz) can transform a predicted mpHFO into a non-mpHFO (**Figure 5i-k**). At a population level, we observed that at least 40% of predicted mpHFO events were transformed to non-mpHFO after stretching the sub-HFO band horizontally by a factor of five (**Supplementary Figure 12**).

Prediction of postoperative seizure outcomes using the classified HFOs:

Using logistic regression with five-fold cross-validation, we found that the resection ratio of mpHFOs ($AUC = 0.64$) outperformed the resection ratio of unclassified HFOs ($AUC = 0.53$) and the traditional expert-driven classification, spkHFO ($AUC = 0.62$) (**Figure 6a**). A multivariable logistic regression incorporating demographic data (age and sex) and the status of SOZ resection showed that the use of mpHFO resection ratio as a primary predictive variable demonstrated slightly better predictive performance than the use of spkHFO resection ratio ($AUC = 0.71$ vs. 0.70) (**Figure 6b**). The random forest trained exclusively with the mpHFO resection ratio demonstrated better predictive performance ($F1 = 0.72$) compared to using unclassified HFOs ($F1 = 0.68$, $p < 0.01$) and spkHFO ($F1 = 0.68$, $p < 0.01$). It also achieved competitive performance compared with predictions based on demographic information and SOZ resection status ($F1 = 0.74$). Furthermore, a comprehensive model that included all features—demographic data, SOZ resection, and mpHFO resection ratio—achieved superior predictive power ($F1 = 0.83$, $p < 0.01$) over models using traditional expert-driven HFO classification ($F1 = 0.81$) (**Supplementary Table 2**). An ablation study, in which we trained random forest only included patients with a higher number of HFOs, demonstrated consistent F1 scores, underscoring the robustness of our framework (**Supplementary Figure 13**).

DISCUSSION

In this study, we developed and implemented a self-supervised deep learning approach to classify pathological HFOs in a large cohort of 185 epilepsy patients who underwent iEEG monitoring with grid or SEEG electrodes across various brain regions. Our approach utilized VAEs to analyze the latent space of HFOs, revealing distinct morphological features that differentiate pathological HFOs (mpHFOs) from their physiological

counterparts. A novel finding was that pathological HFOs exhibited notably high signal intensity within the HFO band at detection, extending across the sub-HFO band (10-80 Hz). This feature was consistently observed across various patient characteristics, including recording sites, pathology, and anatomical locations. Both latent space interpolation and time-domain perturbation further highlighted the critical role of gamma-band activity (30–80 Hz) and the high intensity of HFO band activity in distinguishing mpHFOs from non-mpHFOs. Incorporating the resection status of the mpHFOs into prediction models significantly enhanced the accuracy of postoperative seizure freedom forecasts.

Novel self-supervised approach solves HFO research challenges

HFO research has long faced significant challenges, particularly in differentiating between pathological and physiological HFOs. Despite promising results from numerous retrospective studies,^{5,28} a clinical trial failed to demonstrate the utility of HFOs in improving postoperative seizure outcomes.²⁹ Traditional methods that attempt to identify pathological HFOs, such as associating them with spike-wave discharges,³⁰⁻³² suffer from inconsistencies in expert labeling and poor inter-rater reliability.³³ Moreover, simple analyses of HFO features such as frequency, amplitude, and duration have been ineffective in differentiating pathological from physiological HFOs.^{14,15} While fast ripples (250–500 Hz) may more accurately delineate epileptogenic zones than ripples (80–250 Hz), their low sensitivity complicates the applicability.^{34,35} Region-specific adjustments to HFO detection rates offer some insight into pathological states,^{22,36} but cannot reliably classify individual HFO events.

Recent studies suggest using clinical evidence, such as resection status, seizure outcomes, or functional mapping, to design a weakly supervised framework rather than relying on expert labels.^{9,10,26} As these labels are noisy—not all HFOs in resected areas or the SOZ are pathological—extending this weakly supervised approach requires a large cohort with postoperative outcomes. This approach faces challenges: as more patients undergo SEEG for diagnostics or neuromodulation rather than resection, data for the weakly supervised method is limited. Additionally, variability in defining SOZ and resected regions across institutions may introduce noise in the training data, impacting its applicability.^{11,12}

We addressed these challenges by adopting a fundamentally different, data-driven strategy using VAEs. Unlike prior studies that relied on training neural networks on human-annotated or weak labels,^{9,10,26,37-41} which limited scalability on large datasets and were constrained by the limitation inherent in labeling, our self-supervised model required no such annotations. Our approach builds on the premise that pathological HFOs exhibit distinct morphological characteristics that are separable from physiological ones. The biological plausibility of this hypothesis is grounded in the fact that pathological HFOs arise from abnormal synchronous burst firing, whereas physiological HFOs are generated by inhibitory synchronous postsynaptic potentials^{7,13}. While these differences may be too subtle for traditional signal processing techniques using macroelectrodes, our

VAE model was able to effectively capture and cluster these features within a latent space. These clusters revealed diverse HFO morphologies, enabling direct visualization and latent space interpolations that allowed us to interpret the model's findings. By perturbing the latent space, we identified that the combination of high gamma-band and HFO-band activity correlated strongly with pathological HFOs, a finding further supported by time-domain perturbation.

Our results are compelling, as our deep generative model identified pathological HFOs with features commonly recognized by experts, such as spikes, without relying on subjective "spike" annotations. The identified pathological HFOs were primarily localized around the SOZ, even though the model was trained without SOZ labels. The model objectively revealed increased signal activity in the HFO and gamma bands. The gamma-band EEG signals seemed to emerge as spike-like EEG activity (gamma-spike) in time series data.^{42,43}

Clinical implications

Our findings provide clinically significant insights. Incorporating the resection ratio of mpHFOs into predictive models greatly improved accuracy in forecasting postoperative seizure freedom, outperforming traditional approaches. Our results are consistent with a recent international multicenter study analyzing 109 subjects, demonstrating that the removal of brain regions with HFOs with spikes (spike ripples) correlated better with postoperative seizure outcomes than the removal of unclassified ripples, fast ripples, and spikes.⁴⁴ Moreover, the potential clinical utility is evident as the use of resection ratio of mpHFOs achieves the same performance as the current clinical standards regarding the removal status of SOZ in predicting postoperative outcomes. The mpHFOs can be analyzed from short interictal EEG data, offering the potential to reduce the duration of EEG monitoring, hospital stays, and associated costs for the patient. Furthermore, combining the resection status of the SOZ with the proportion of mpHFO resection further enhanced the prediction, suggesting an additive effect when mpHFOs are combined with the current clinical standard.

Another notable discovery was that non-pathological HFOs originating from the occipital lobe displayed distinct morphological features compared to HFOs from other brain regions. Physiological HFOs were reportedly abundant in the occipital lobe^{45,46} and also showed distinct coupling with slow waves.⁴⁷ This study added essential findings in the literature to establish the unique morphology of HFOs originating in the occipital lobe. These findings could potentially overcome the limitation faced by the HFO trial, which necessitated the exclusion of subjects with occipital lobe epilepsy due to the likelihood of abundant physiological HFOs in such patients.²⁹

Limitations and further work

While our results are promising, several limitations should be considered. First, the study was conducted using macroelectrode recordings, which may not fully capture the fine-grained neurophysiological mechanisms at

the single-neuron level. Although our cohort included 185 patients, only 18 were monitored with SEEG, limiting our ability to sample from deeper brain areas. With more balanced coverage of both superficial and deep areas, network analysis to account for HFO propagation may provide better accuracy in the prediction of postoperative surgical outcomes.⁴⁸ Additionally, the study focused primarily on pediatric patients, so expanding the adult population is needed for generalization. The EEG data consisted mostly of short, five-minute recordings, typically around five minutes from the initial night during sleep, with a sampling frequency limited to 1,000 Hz (Detroit dataset), which restricted fast ripple (250–500 Hz) analysis. Although our results suggest that the peak frequency of HFOs did not affect pathological classification, further investigation of the fast ripple band will be needed. Longer, multi-day recordings might reveal HFOs with potentially varying morphologies over time.⁴⁹ The vigilance state should also be considered,⁵⁰ as morphological differences between various sleep stages and wakefulness remain under-investigated. Finally, our sample size may not fully capture subtle HFO morphology differences across epilepsy pathology subtypes, such as focal cortical dysplasia or tumors.

Our data and analysis code are now publicly available to enable other research groups to replicate our findings. Moving forward, we plan to collaborate with additional institutions to test the generalizability of our approach. As we establish definitions for pathological HFOs across different anatomical regions, this data can be integrated with other modalities, such as neuroimaging, to guide surgical resections and neuromodulation strategies.

FUNDING

The authors have no conflict of interest to disclose. HN is supported by the National Institute of Neurological Disorders and Stroke (NINDS) K23NS128318, the Sudha Neelakantan & Venky Harinarayan Charitable Fund, the Elsie and Isaac Fogelman Endowment, and the UCLA Children's Discovery and Innovation Institute (CDI) Junior Faculty Career Development Grant (#CDI-SEED-010124). AD is supported by the Uehara Memorial Foundation and the SENSHIN Medical Research Foundation. EA is supported by the National Institute of Health (R01NS064033). RS serves on scientific advisory boards and speakers bureaus and has received honoraria and funding for travel from Eisai, Greenwich Biosciences, UCB Pharma, Sunovion, Supernus, Lundbeck Pharma, Liva Nova, and West Therapeutics (advisory only); receives royalties from the publication of Pellock's Pediatric Neurology (Demos Publishing, 2016) and Epilepsy: Mechanisms, Models, and Translational Perspectives (CRC Press, 2011). RS is also supported by the Sudha Neelakantan & Venky Harinarayan Charitable Fund. RJS is supported by the NINDS R01NS106957, R01NS033310, and R01NS127524. JEJ is supported by NINDS U54NS100064 and R01NS033310. RJS and JEJ are supported by the Christina Louise George Trust. The research described was also supported by NIH/National Center for Advancing Translational Science (NCATS) UCLA CTSI Grant Number UL1TR001881.

AUTHOR CONTRIBUTION

Study concept/design/supervision: VR, HN

Data collection/analysis: YZ, AD, LL, NK, YD, SO, SK, TM, CD, SAH, JXQ, NS, AF, MSS,

Manuscript draft: YZ, AD, SO, SK, VA, HN

Manuscript revision: YZ, AD, SO, SK, RS, RJS, JE, EA, VR, HN

COMPETING INTERESTS

The authors have no conflict of interest to disclose.

DATA AVAILABILITY

Anonymized EEG data and metadata, including labels (channel's resection status, SOZ, patients' demographics, seizure outcomes, and pathology) used in this study are available on the OpenNEURO website (<https://openneuro.org/datasets/ds005398>). The Python-based code used in this study will also be available at (<https://github.com/roychowdhuryresearch/HFO-VAE>). One can train and test the deep learning algorithm from their data and confirm our methods' validity and utility.

FIGURE LEGENDS

Figure 1. Study flow. (a) Spatial distribution of intracranial electrodes: Electrode contact locations within the standardized MNI brain space from various views (Lateral Left, Lateral Right, Anterior, Posterior). (b) Variational Autoencoder (VAE) training: Time-frequency plots representing HFOs serve as input into the VAE, which outputs a reconstructed image. The VAE's encoder generates a latent distribution of mean and variance while the decoder reconstructs the time-frequency plot from a sampled latent vector from the distribution. The loss function is a combination of perceptual loss (to capture morphological differences) and KL divergence (measuring the latent distribution's deviation from a normal distribution). (c) HFO classification pipeline: A two-stage, morphology-based classification process uses Gaussian Mixture Models (GMMs) for unsupervised learning. The first stage identifies artifacts (mArtifact) by latent codes and reconstruction loss; the second stage distinguishes putative pathological HFOs (mpHFOs) cluster; the cluster with a higher resection percentage in seizure-free patients after resection was deemed pathological. This process trains two unsupervised classifiers to be used on the test set. (d) Interpretability analysis. Left: Latent space clustering, visualized via t-SNE, groups clinically relevant HFO classes, facilitating interpretation through consistency with the HFO classification. Right: Dimensional interpolation in latent space discovers specific neurophysiological features in reconstructed images, providing a bridge between clinical insights and the VAE's feature representations.

Figure 2. Characterization of pathological HFOs (mpHFOs) based on the self-supervised VAE algorithm. (a). Projected latent space, color-coded by predicted results (mpHFO, non-mpHFO, and mArtifact) from VAE-based HFO morphology inference pipeline on one fold, shows the 2D projected eight-dimensional latent codes by the t-SNE. (b). The same latent space is color-coded by conventional HFO classification (spkHFO, non-spkHFO, and artifact). (c) HFO rates (number of HFO detections [count/channel/min]) of mpHFO and non-mpHFO are plotted in box plots based on the location (SOZ versus non-SOZ) across three datasets (outliers were removed for better visualization quality). The rate of mpHFO (count/channel/min) was higher in the SOZ than in the non-SOZ. The rates of non-mpHFOs (count/channel/min) did not differ between the SOZ and non-SOZ (*: $p < 0.05$; **: $p < 0.01$; ***: $p < 0.001$). (d) Morphological analysis of the time-frequency plot for an example subject in Detroit grid/strip, UCLA SEEG and UCLA grid/strip datasets. The pathological counterparts (mpHFOs) have higher values throughout the HFO band (> 80 Hz), around the center point (0 ms, where HFOs were detected) than non-mpHFOs; furthermore, higher values of mpHFOs at the sub-HFO band (10-80 Hz) throughout the time window compared to non-mpHFOs are exhibited. (e) The overall template (mean) of all subjects resembles a "cone-shaped" (pixel comparisons that were significantly higher in mpHFOs than non-mpHFOs in more than 50% of patients were colored orange). (f) Time-frequency plot of an example predicted mpHFO. (g) EEG tracing of the same mpHFO with the detected HFO part colored in red. (h) EEG tracing bandpassed between 10 and 80 Hz

of the same mpHFO with HFO detection colored in red. (i/j/k) An example predicted non-mpHFO presented in the same fashion as the mpHFO example. Note the presence of a spike-wave activity in EEG in the mpHFO but not in the non-mpHFO.

Figure 3. Investigating potential heterogeneity of HFO morphology based on variables. (a) Visualization of the latent space for HFOs, color-coded by different recording sites/types (UCLA SEEG, UCLA grid/strip, and Detroit grid/strip) on one fold. (b) Across five-fold, the classifiers trained using the actual recording sites/type labels (Real) did not show significantly better accuracy than those trained by using the permuted labels (Random). (c) Visualization of the latent space for HFOs color-coded by different sexes (male and female) on a specific fold. (d) Across five-fold, the classifiers trained using the actual sex labels (Real) did not show significantly better accuracy than those trained by permuted labels (Random). (e) Visualization of the latent space for HFOs color-coded by different age groups (0-5, 6-10, 11-15, 16-20, and 21+) on one fold. (f) Across five-fold, the classifiers trained using the actual age group labels (Real) did not show significantly better accuracy than those trained by label permuted data (Random). (g) Visualization of the latent space for HFOs color-coded by different pathologies (HS, FCD, Tumor, and Others) on one fold. (h) Across five-fold, the classifiers trained using actual pathology labels (Real) did not show significantly better accuracy than those trained by label-permuted data (Random).

Figure 4. Morphological investigations of HFOs from various anatomical regions. (a) Visualization of the latent space for HFOs from preserved brain regions of post-surgical, seizure-free subjects, color-coded by anatomical locations (frontal, temporal, parietal, occipital, and limbic regions) on one fold. (b) Across five-fold, the classifiers trained using actual anatomical location label (Real) showed significantly better ($p = 6.67e-10$) accuracy than those trained by permuted label (Random) (Real mean=0.286, std= 0.046, Random mean = 0.230, std= 0.033). (c) Averaged confusion matrix on the test set across five trials and five-fold ($n=25$ trials) using actual anatomical locations for HFOs from preserved brain regions of subjects who achieved postoperative seizure freedom. Note that HFOs from the occipital region were distinguishable. (d) Averaged time-frequency plots for each anatomical location for HFOs from each brain region. Note that HFOs from the occipital region exhibited distinct features on the time-frequency plot. (e) Visualization of the latent space for HFOs from SOZ channels, color-coded by anatomical locations. (f) Across five-fold, for HFOs from SOZ channels, the classifiers trained using the anatomical location label (Real) did not show significantly better ($p = 0.090$) accuracy than those trained by permuted label (Random) (Real mean=0.241, std=0.043, Random mean = 0.23, std=0.027). (g) Averaged confusion matrix on the test set across five trials and five-fold ($n=25$) using actual anatomical locations for HFOs from SOZ channels. Note that HFOs from the SOZ were indistinguishable from any anatomical origin. (h)

Averaged time-frequency plots for each anatomical location for HFOs from the SOZ channels. Note that HFOs from the SOZ exhibited similar features within time-frequency plots across the anatomical regions.

Figure 5. Disentanglement of the latent space to establish neurophysiological characteristics of pathological HFOs (mpHFOs). (a) Pathological dimension visualization. This panel illustrates the VAE-identified latent dimension, which enables separation between mpHFOs and non-mpHFOs. (b) A traversal from the lower to the upper percentile of this dimension revealed morphological evolution from non-mpHFO to mpHFO characteristics for both mpHFO (orange) and non-mpHFO (blue) representatives in the decoded output, depicted in the image sequence. (c) Power trend within the pathological dimension at the population level. The box plot aggregates the percentage of power in the gamma band and HFO band (> 30Hz) within the designated pathological template (the cone-shaped) region of decoded images, showing an ascending trend with higher values, as indicated by the fitted median line. (d) Distribution of model probability scores for each sample. The red circles indicate the mean probability scores, showing increased confidence in the model as the value of the pathological dimension increases. (e) Beta band dimension visualization. This latent space represented the beta-band component of HFOs at 10-30 Hz, separated by mpHFO and non-mpHFO prediction. (f) The output of the decoder traversing the dimension, displayed in the image sequence, showed an increased trend in beta band power from lower to upper percentiles of the value of that dimension. (g) At the population level, the box plot demonstrated a positive correlation between beta band dimension values and beta band power within a cone-shaped template in decoded images, with a line fit illustrating the median trend. (h) Model probability scores distribution corresponding to each sample, where the mean of the probability marked as red circles, showed the average confidence of perturbed events was around 0.5. (i) An example of predicted mpHFO tracing, with corresponding time-frequency plot, with $P_{\text{mpHFO}}=0.983$, (j) By stretching the signal in the subHFO band (10-80 Hz) by a factor of 3, the confidence of mpHFO went down to 0.411. (k) Further stretching the signal in the subHFO band by a factor of 5, this event becomes more toward non-mpHFO with $P_{\text{mpHFO}}=0.273$.

Figure 6. Clinical validation: resection status of pathological HFOs (mpHFOs) helps predict postoperative seizure outcomes. (a) AUCs (area under the curve) of logistic regression (a single-variable classifier) using resection ratios as a variable to predict postoperative seizure freedom are shown based on different types of HFO resection ratios: HFO (unclassified HFO detection), spkHFO (HFO with spike), and mpHFO (pathological HFO defined by the VAE algorithm). (b) AUCs from multivariable logistic regression models with different types of HFO resection ratios as the main predictive variable while incorporating subject-wise demographic information (baseline demographics: age and sex) are shown. As an additional predictive variable, the resection status of SOZ was also included. Note that combining the baseline demographics (base), SOZ resection status (soz), and resection ratio of mpHFO (mpHFO) provided the most favorable performance (base.+soz+mpHFO, AUC=0.71).

(c) The mean F1 scores (F1) and standard error of the mean for the random forest models, trained on the training subjects using five-fold cross-validation and evaluated on the test subjects across the five folds and using different features, are shown. Note that the resection ratio of mpHFO achieved a competitive predictive performance compared to the current clinical standard (SOZ resection status). By combining all the features (baseline demographics, mpHFO resection ratio, and SOZ resection status), the model achieved high performance with an F1 score of 0.832.

REFERENCES

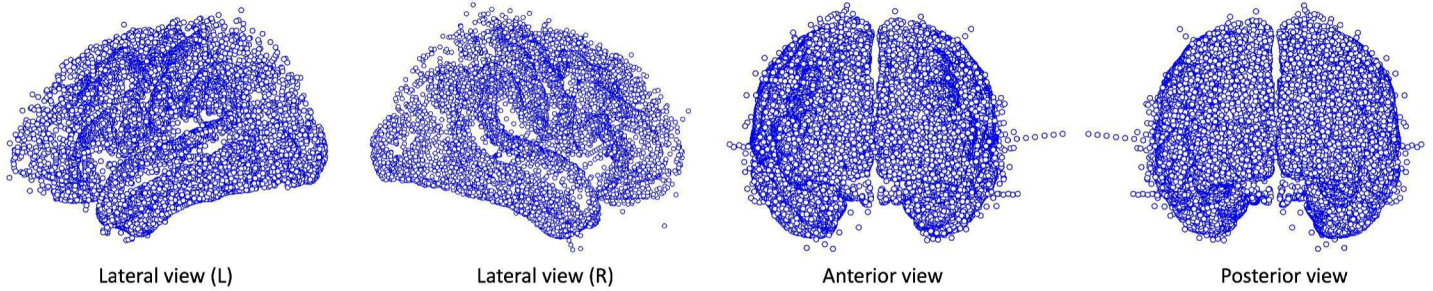
1. West S, Nevitt SJ, Cotton J, et al. Surgery for epilepsy. *Cochrane Database Syst Rev*. Jun 25 2019;6(6):Cd010541. doi:10.1002/14651858.CD010541.pub3
2. Bragin A, Engel J, Jr., Wilson CL, Fried I, Mathern GW. Hippocampal and entorhinal cortex high-frequency oscillations (100--500 Hz) in human epileptic brain and in kainic acid--treated rats with chronic seizures. *Epilepsia*. Feb 1999;40(2):127-37.
3. Worrell GA, Parish L, Cranstoun SD, Jonas R, Baltuch G, Litt B. High-frequency oscillations and seizure generation in neocortical epilepsy. *Brain*. Jul 2004;127(Pt 7):1496-506. doi:10.1093/brain/awh149
4. Jirsch JD, Urrestarazu E, LeVan P, Olivier A, Dubeau F, Gotman J. High-frequency oscillations during human focal seizures. *Brain*. Jun 2006;129(Pt 6):1593-608. doi:10.1093/brain/awl085
5. Jacobs J, Zijlmans M, Zelmann R, et al. High-frequency electroencephalographic oscillations correlate with outcome of epilepsy surgery. *Annals of neurology*. Feb 2010;67(2):209-20. doi:10.1002/ana.21847
6. van 't Klooster MA, van Klink NEC, Zweiphenning W, et al. Tailoring epilepsy surgery with fast ripples in the intraoperative electrocorticogram. *Annals of neurology*. May 2017;81(5):664-676. doi:10.1002/ana.24928
7. Zijlmans M, Jiruska P, Zelmann R, Leijten FS, Jefferys JG, Gotman J. High-frequency oscillations as a new biomarker in epilepsy. *Annals of neurology*. Feb 2012;71(2):169-78. doi:10.1002/ana.22548
8. LeCun Y, Bengio Y, Hinton G. Deep learning. *Nature*. May 28 2015;521(7553):436-44. doi:10.1038/nature14539
9. Zhang Y, Lu Q, Monsoor T, et al. Refining epileptogenic high-frequency oscillations using deep learning: a reverse engineering approach. *Brain Commun*. 2022;4(1):fcab267. doi:10.1093/braincomms/fcab267
10. Zhang Y, Chung H, Ngo JP, et al. Characterizing physiological high-frequency oscillations using deep learning. *J Neural Eng*. Dec 7 2022;19(6)doi:10.1088/1741-2552/aca4fa
11. Kini LG, Bernabei JM, Mikhail F, et al. Virtual resection predicts surgical outcome for drug-resistant epilepsy. *Brain*. Dec 1 2019;142(12):3892-3905. doi:10.1093/brain/awz303
12. Thomas J, Abdallah C, Cai Z, et al. Investigating current clinical opinions in stereoelectroencephalography-informed epilepsy surgery. *Epilepsia*. Aug 3 2024;doi:10.1111/epi.18076
13. Jefferys JG, Menendez de la Prida L, Wendling F, et al. Mechanisms of physiological and epileptic HFO generation. *Prog Neurobiol*. Sep 2012;98(3):250-64. doi:10.1016/j.pneurobio.2012.02.005
14. Matsumoto A, Brinkmann BH, Matthew Stead S, et al. Pathological and physiological high-frequency oscillations in focal human epilepsy. *J Neurophysiol*. Oct 2013;110(8):1958-64. doi:10.1152/jn.00341.2013
15. Cimbalnik J, Brinkmann B, Kremen V, et al. Physiological and pathological high frequency oscillations in focal epilepsy. *Ann Clin Transl Neurol*. Sep 2018;5(9):1062-1076. doi:10.1002/acn3.618
16. Kingma DP, Welling M. Auto-encoding variational bayes. *arXiv preprint arXiv:1312.6114*. 2013;

17. Kenton JDM-WC, Toutanova LK. Bert: Pre-training of deep bidirectional transformers for language understanding. 2019:2.
18. Razavi A, Oord Avd, Vinyals O. Generating Diverse High-Fidelity Images with VQ-VAE-2. *arXiv preprint arXiv:190600446*. 2019;
19. Lu Q, Zhang Y, Lu M, Roychowdhury V. Action-conditioned on-demand motion generation. 2022:2249-2257.
20. Dai M, Zheng D, Na R, Wang S, Zhang S. EEG Classification of Motor Imagery Using a Novel Deep Learning Framework. *Sensors*. Jan 29 2019;19(3)doi:10.3390/s19030551
21. Tian C, Ma Y, Cammon J, Fang F, Zhang Y, Meng M. Dual-Encoder VAE-GAN With Spatiotemporal Features for Emotional EEG Data Augmentation. *IEEE Trans Neural Syst Rehabil Eng*. 2023;31:2018-2027. doi:10.1109/tnsre.2023.3266810
22. Kuroda N, Sonoda M, Miyakoshi M, et al. Objective interictal electrophysiology biomarkers optimize prediction of epilepsy surgery outcome. *Brain Commun*. 2021;3(2):fcab042. doi:10.1093/braincomms/fcab042
23. Klein A, Tourville J. 101 labeled brain images and a consistent human cortical labeling protocol. *Front Neurosci*. 2012;6:171. doi:10.3389/fnins.2012.00171
24. Wu J, Ngo GH, Greve D, et al. Accurate nonlinear mapping between MNI volumetric and FreeSurfer surface coordinate systems. *Human brain mapping*. Sep 2018;39(9):3793-3808. doi:10.1002/hbm.24213
25. Zhang Y, Liu L, Ding Y, et al. PyHFO: lightweight deep learning-powered end-to-end high-frequency oscillations analysis application. *J Neural Eng*. May 9 2024;doi:10.1088/1741-2552/ad4916
26. Monsoor T, Zhang Y, Daida A, et al. Optimizing detection and deep learning-based classification of pathological high-frequency oscillations in epilepsy. *Clinical neurophysiology : official journal of the International Federation of Clinical Neurophysiology*. Aug 9 2023;154:129-140. doi:10.1016/j.clinph.2023.07.012
27. Lucas A, Revell A, Davis KA. Artificial intelligence in epilepsy - applications and pathways to the clinic. *Nat Rev Neurol*. May 8 2024;doi:10.1038/s41582-024-00965-9
28. Wu JY, Sankar R, Lerner JT, Matsumoto JH, Vinters HV, Mathern GW. Removing interictal fast ripples on electrocorticography linked with seizure freedom in children. *Neurology*. Nov 09 2010;75(19):1686-94. doi:10.1212/WNL.0b013e3181fc27d0
29. Zweiphenning W, Klooster MAV, van Klink NEC, et al. Intraoperative electrocorticography using high-frequency oscillations or spikes to tailor epilepsy surgery in the Netherlands (the HFO trial): a randomised, single-blind, adaptive non-inferiority trial. *Lancet neurology*. Nov 2022;21(11):982-993. doi:10.1016/s1474-4422(22)00311-8

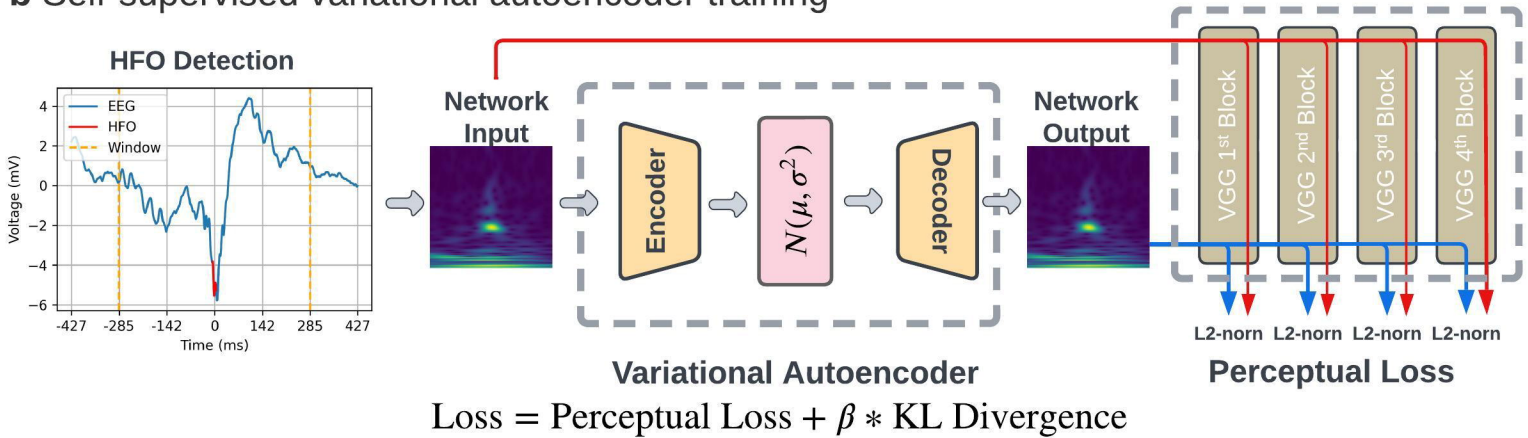
30. Weiss SA, Orosz I, Salamon N, et al. Ripples on spikes show increased phase-amplitude coupling in mesial temporal lobe epilepsy seizure-onset zones. *Epilepsia*. Nov 2016;57(11):1916-1930. doi:10.1111/epi.13572
31. Song I, Orosz I, Chervoneva I, et al. Bimodal coupling of ripples and slower oscillations during sleep in patients with focal epilepsy. *Epilepsia*. Nov 2017;58(11):1972-1984. doi:10.1111/epi.13912
32. Cai Z, Sohrabpour A, Jiang H, et al. Noninvasive high-frequency oscillations riding spikes delineates epileptogenic sources. *Proceedings of the National Academy of Sciences of the United States of America*. Apr 27 2021;118(17)doi:10.1073/pnas.2011130118
33. Nariai H, Wu JY, Bernardo D, Fallah A, Sankar R, Hussain SA. Interrater reliability in visual identification of interictal high-frequency oscillations on electrocorticography and scalp EEG. *Epilepsia open*. Dec 2018;3(Suppl Suppl 2):127-132. doi:10.1002/epi4.12266
34. Roehri N, Pizzo F, Lagarde S, et al. High-frequency oscillations are not better biomarkers of epileptogenic tissues than spikes. *Annals of neurology*. Jan 2018;83(1):84-97. doi:10.1002/ana.25124
35. Nevalainen P, von Ellenrieder N, Klimeš P, Dubeau F, Frauscher B, Gotman J. Association of fast ripples on intracranial EEG and outcomes after epilepsy surgery. *Neurology*. Oct 20 2020;95(16):e2235-e2245. doi:10.1212/wnl.0000000000010468
36. Zweiphenning W, von Ellenrieder N, Dubeau F, et al. Correcting for physiological ripples improves epileptic focus identification and outcome prediction. *Epilepsia*. Feb 2022;63(2):483-496. doi:10.1111/epi.17145
37. Zhao B, Hu W, Zhang C, et al. Integrated Automatic Detection, Classification and Imaging of High Frequency Oscillations With Stereoelectroencephalography. *Front Neurosci*. 2020;14:546. doi:10.3389/fnins.2020.00546
38. Besheli BF, Sha Z, Gavvala JR, et al. A sparse representation strategy to eliminate pseudo-HFO events from intracranial EEG for seizure onset zone localization. *J Neural Eng*. Aug 24 2022;19(4)doi:10.1088/1741-2552/ac8766
39. Medvedev AV, Agoureeva GI, Murro AM. A Long Short-Term Memory neural network for the detection of epileptiform spikes and high frequency oscillations. *Sci Rep*. Dec 18 2019;9(1):19374. doi:10.1038/s41598-019-55861-w
40. Nejedly P, Kremen V, Sladky V, et al. Exploiting Graphoelements and Convolutional Neural Networks with Long Short Term Memory for Classification of the Human Electroencephalogram. *Sci Rep*. Aug 6 2019;9(1):11383. doi:10.1038/s41598-019-47854-6
41. Guo J, Xiao N, Li H, et al. Transformer-Based High-Frequency Oscillation Signal Detection on Magnetoencephalography From Epileptic Patients. *Front Mol Biosci*. 2022;9:822810. doi:10.3389/fmolb.2022.822810

42. Latreille V, Corbin-Lapointe J, Peter-Derex L, Thomas J, Lina JM, Frauscher B. Oscillatory and nonoscillatory sleep electroencephalographic biomarkers of the epileptic network. *Epilepsia*. Aug 24 2024;doi:10.1111/epi.18088
43. Klimes P, Nejedly P, Hrtonova V, et al. Interictal stereo-electroencephalography features below 45 Hz are sufficient for correct localization of the epileptogenic zone and postsurgical outcome prediction. *Epilepsia*. Aug 24 2024;doi:10.1111/epi.18081
44. Shi W, Shaw D, Walsh KG, et al. Spike ripples localize the epileptogenic zone best: an international intracranial study. *Brain*. Jul 5 2024;147(7):2496-2506. doi:10.1093/brain/awae037
45. Frauscher B, von Ellenrieder N, Zelmann R, et al. High-Frequency Oscillations in the Normal Human Brain. *Annals of neurology*. Sep 2018;84(3):374-385. doi:10.1002/ana.25304
46. Guragain H, Cimbalnik J, Stead M, et al. Spatial variation in high-frequency oscillation rates and amplitudes in intracranial EEG. *Neurology*. Feb 20 2018;90(8):e639-e646. doi:10.1212/wnl.0000000000004998
47. Sakakura K, Kuroda N, Sonoda M, et al. Developmental atlas of phase-amplitude coupling between physiologic high-frequency oscillations and slow waves. *Nature communications*. Oct 13 2023;14(1):6435. doi:10.1038/s41467-023-42091-y
48. Tamilya E, Park EH, Percivati S, et al. Surgical resection of ripple onset predicts outcome in pediatric epilepsy. *Annals of neurology*. Sep 2018;84(3):331-346. doi:10.1002/ana.25295
49. Gliske SV, Irwin ZT, Chestek C, et al. Variability in the location of high frequency oscillations during prolonged intracranial EEG recordings. *Nature communications*. Jun 1 2018;9(1):2155. doi:10.1038/s41467-018-04549-2
50. von Ellenrieder N, Dubeau F, Gotman J, Frauscher B. Physiological and pathological high-frequency oscillations have distinct sleep-homeostatic properties. *NeuroImage Clinical*. 2017;14:566-573. doi:10.1016/j.nicl.2017.02.018

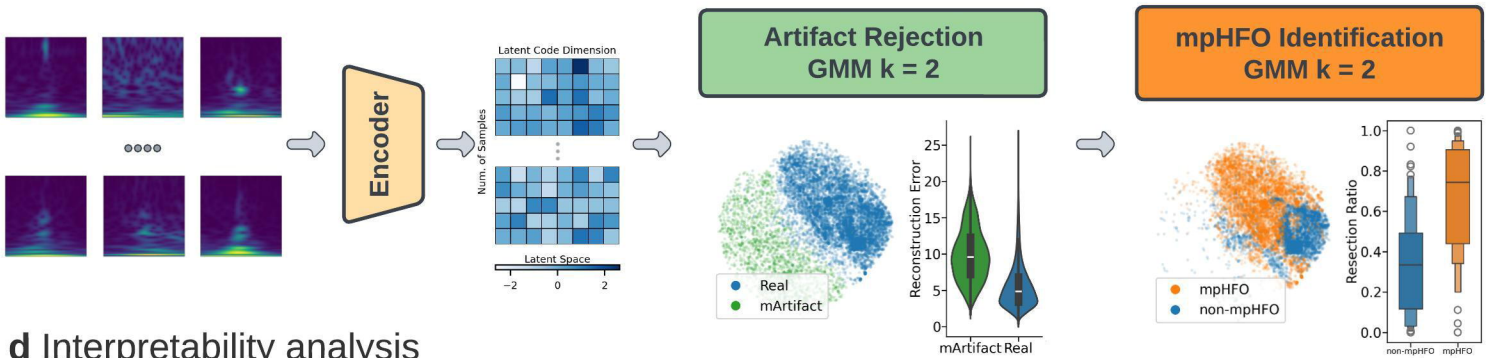
a Spatial distribution of intracranial electrode sampling



b Self-supervised variational autoencoder training

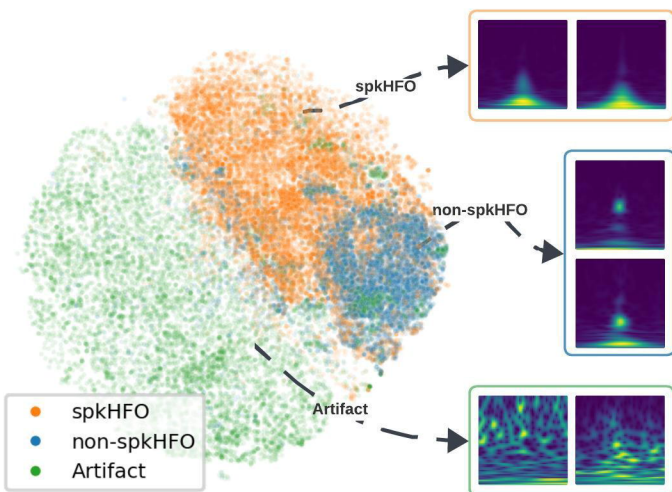


c Morphology-based HFO classification

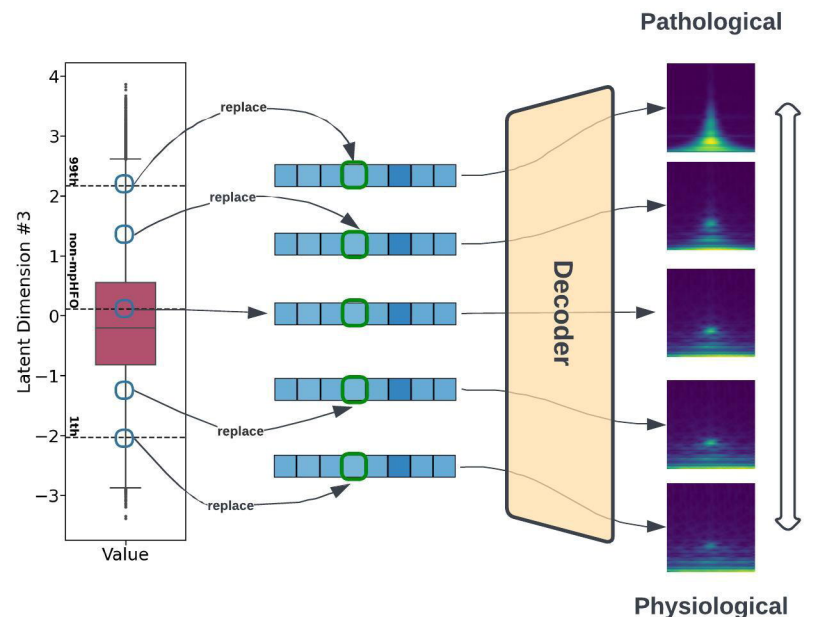


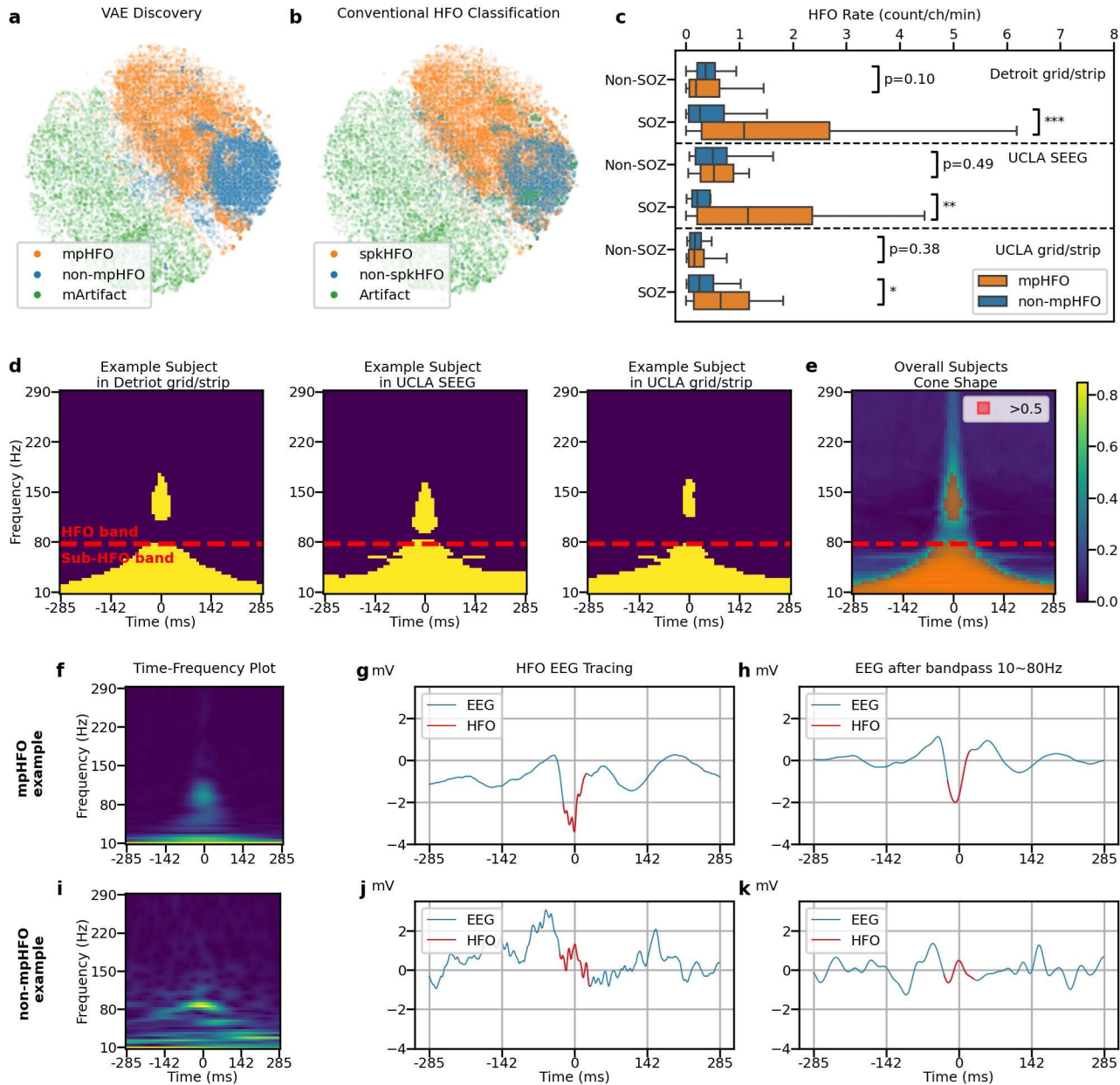
d Interpretability analysis

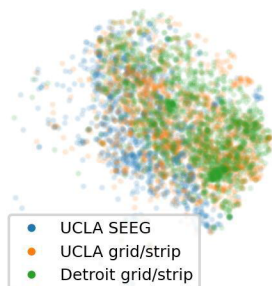
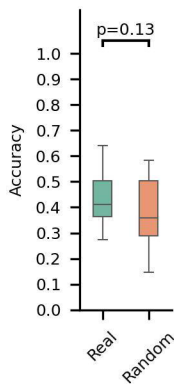
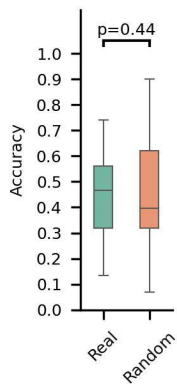
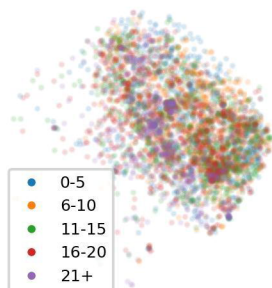
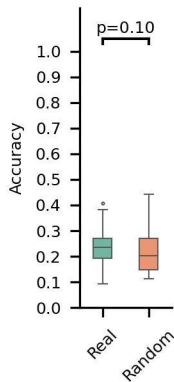
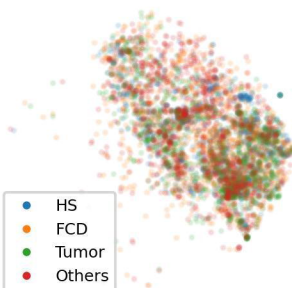
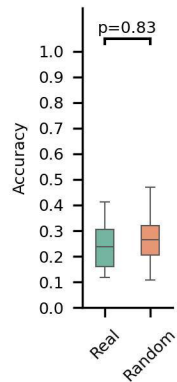
Clinical interpretation of latent space clustering



Neurophysiological interpretation of latent space disentanglement

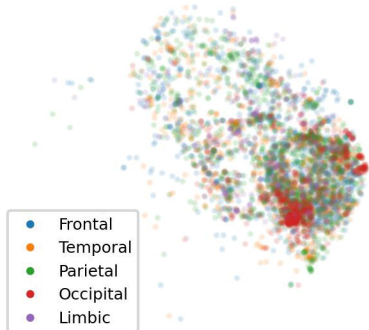




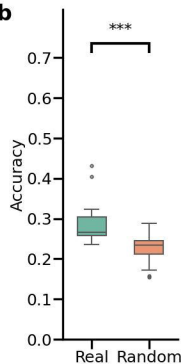
Recording sites/types**a****b****Sex****c****d****Age groups****e****f****Pathologies****g****h**

HFOs from preserved brain regions of post-surgical, seizure-free subjects

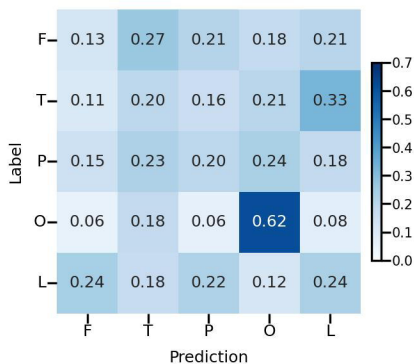
a



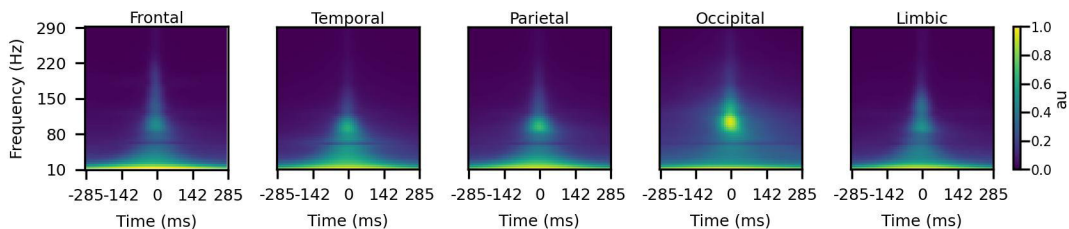
b



c

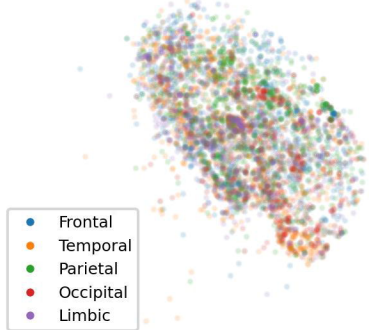


d

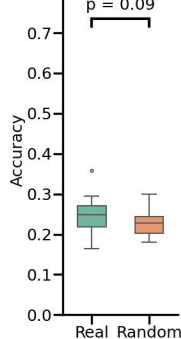


HFOs from SOZ channels

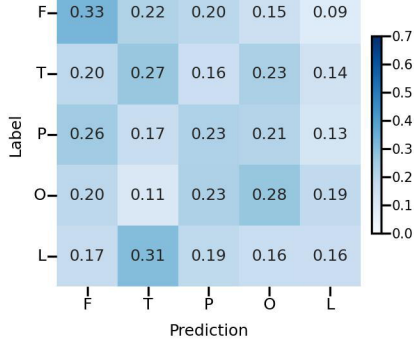
e



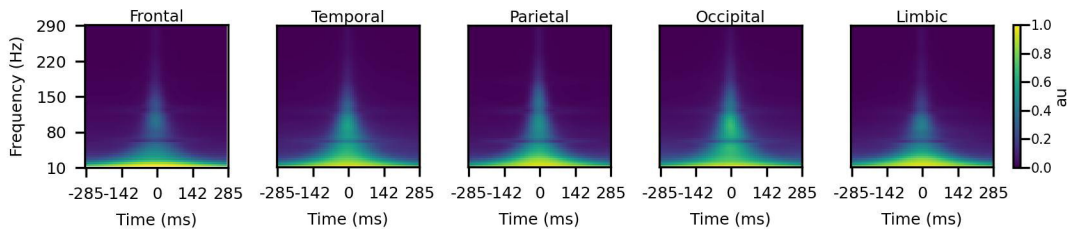
f

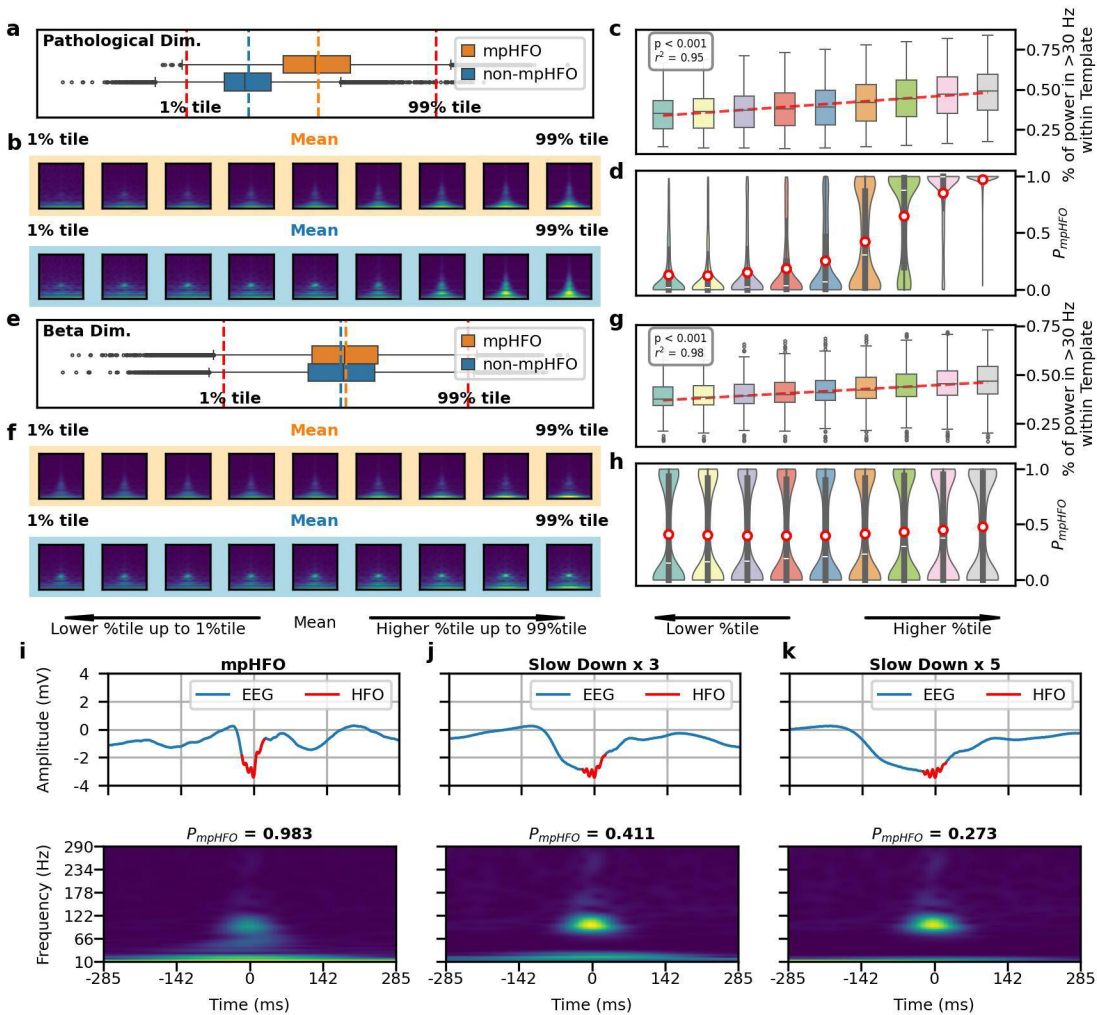


g



h





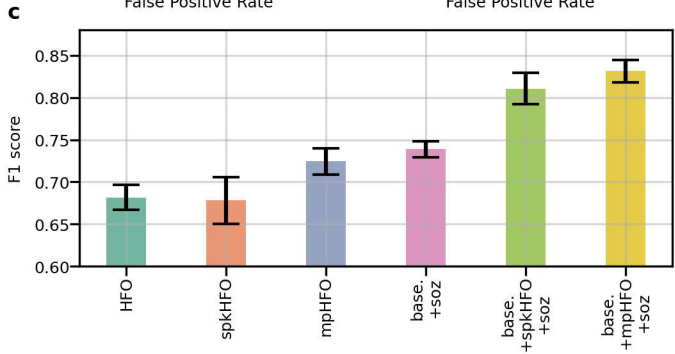
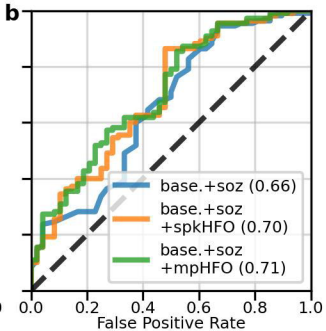
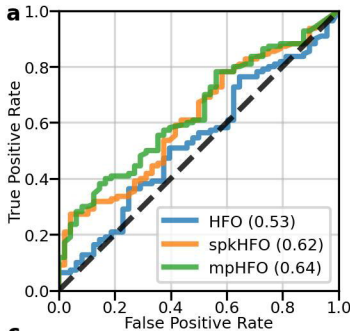


Table 1: Patient Demographics

	UCLA	Detroit	All	
Number of patients	50	135	185	
Median age in years (range)	14.5 (2-28)	12.0 (4-44)	13 (2-44)	
Proportion of female (%)	24 (48.0%)	67 (49.6%)	91 (49.2%)	
Proportion of grid case (vs. SEEG) (%)	32 (64.0%)	135 (100.0%)	167 (90.3%)	
Sampled hemisphere (%)	Left	21 (42.0%)	61 (45.19%)	82 (44.3%)
	Right	11 (22.0%)	51 (37.78%)	62 (33.5%)
	Both	18 (36.0%)	23 (17.04%)	41 (22.2%)
Seizure onset zone	Frontal	24	42	66
	Temporal	16	63	79
	Parietal	22	49	71
	Occipital	4	23	27
	Limbic	18	59	77
Patients who underwent resection [#]	27 (54.0%)	135 (100%)	162 (87.6%)	
Patients with postoperative seizure-freedom (%) [#]	18 (66.7%)	95 (70.4%)	113 (69.8%)	
Pathology (%) [*]	Focal cortical dysplasia	18 (66.7%)	49 (36.3%)	67 (41.4%)
	Hippocampal sclerosis	0 (0.0%)	11 (8.15%)	11 (6.8%)
	Tumor	3 (11.1%)	28 (20.74%)	31 (19.1%)
	Others	6 (22.2%)	47 (34.81%)	53 (32.7%)

*Pathology was considered only in resected patients.

[#]Only three patients in SEEG were resected. Therefore, they were excluded from the outcome analysis.

Table 2: Spatial distribution of intracranial electrode sampling

Region of Interest (ROI)	No. of contacts Left	No. of contacts Right	No. of contacts Total	Proportion of Grid contacts (%)	Proportion of SEEG contacts (%)	No. of SOZ contacts	No. of non-epileptogenic contacts*	HFO rate at SOZ (/min)[#]	HFO rate at non-epileptogenic contacts (/min)[#]
Frontal:	3197	3074	6271	95.39	4.61	437	3015	3.60	1.08
caudal middle frontal	477	400	877	97.38	2.62	52	442	2.77	1.10
frontal pole	2	11	13	100	0	1	3	NA	NA
paracentral	71	99	170	98.82	1.18	12	93	5.68	1.31
pars opercularis	325	203	528	95.27	4.73	33	292	3.14	1.31
pars orbitalis	137	162	299	97.99	2.01	31	118	2.24	1.28
pars triangularis	265	295	560	92.32	7.68	51	256	3.09	1.05
precentral	920	797	1717	95.92	4.08	71	962	6.35	1.03
rostral middle frontal	613	629	1242	95.09	4.91	116	517	2.84	1.04
superior frontal	387	478	865	93.18	6.82	70	332	3.26	1.00
Temporal:	2707	2128	4835	93.9	6.1	464	1864	2.99	1.05
fusiform	481	391	872	97.82	2.18	108	360	2.56	1.02
inferior temporal	469	395	864	97.11	2.89	92	302	3.76	1.06
middle temporal	720	526	1246	89.41	10.59	99	469	2.51	0.98
superior temporal	876	652	1528	92.87	7.13	115	639	3.35	1.04
temporal pole	158	154	312	100	0	46	94	2.74	1.52
transverse temporal	2	10	12	16.67	83.33	4	0	NA	NA
Parietal:	2231	1936	4167	96.02	3.98	393	1933	5.40	1.22
inferior parietal	314	353	667	95.95	4.05	81	215	3.67	1.19
postcentral	832	661	1493	97.19	2.81	91	806	7.17	0.94
precuneus	137	142	279	96.42	3.58	31	144	4.91	1.14
superior parietal	237	173	410	92.2	7.8	48	142	4.42	1.54
supramarginal	711	607	1318	95.83	4.17	142	626	5.83	1.44
Occipital	806	670	1476	98.98	1.02	135	653	3.19	0.81
cuneus	79	62	141	100	0	17	60	4.04	0.87
lateral occipital	504	356	860	98.84	1.16	78	365	3.13	0.87

	lingual	219	249	468	99.79	0.21	40	226	2.95	0.68
Limbic		808	708	1516	82.19	17.81	241	495	2.07	1.28
	hippocampus	32	28	60	0	100	9	7	1.65	1.23
	amygdala	18	14	32	0	100	0	4	NA	NA
	caudal anterior cingulate	26	28	54	55.56	44.44	5	18	3.51	0.66
	entorhinal	164	169	333	99.7	0.3	83	89	1.86	2.15
	insula	40	52	92	0	100	17	21	1.22	0.63
	isthmus cingulate	66	59	125	97.6	2.4	8	55	0.73	1.62
	lateral orbitofrontal	226	179	405	94.81	5.19	50	155	2.42	1.09
	medial orbitofrontal	49	36	85	94.12	5.88	8	37	1.66	1.25
	parahippocampal	104	80	184	96.2	3.8	44	57	1.69	1.37
	posterior cingulate	68	48	116	89.66	10.34	10	49	4.77	0.93
	rostral anterior cingulate	15	15	30	56.67	43.33	7	3	2.67	NA

*Non-epileptogenic contacts were defined as EEG contacts covering spared brain regions in patients who achieved postoperative seizure freedom

ROIs with contacts less than 5 were removed from the analysis